Ultrahigh energy density BeN monolayer: A nodal-line semimetal anode for Li-ion batteries

Shuyi Lin,[1,2] Meiling Xu,[1,*] Feilong Wang,[1] Jian Hao,[1,†] and Yinwei Li[1]

[1]*Laboratory of Quantum Functional Materials Design and Application, School of Physics and Electronic Engineering, Jiangsu Normal University, Xuzhou 221116, China*

[2]*Department of Applied Physics, The Hong Kong Polytechnic University, Hunghom, Hong Kong, 999077, China*

(Received 17 August 2023; accepted 12 December 2023; published 10 January 2024)

Topological quantum materials have significant potential for application as anode materials due to their intrinsically high electronic conductivity against perturbation from defects or impurities. In this work, we utilize a combination of a swarm-intelligence structure search method and first-principles calculations to predict the global minimum of a BeN monolayer, suggesting it as a promising nodal-line semimetal anode for Li-ion batteries. BeN anode demonstrates a substantial specific capacity of 3489 mAh/g and a low average open-circuit voltage of 0.15 V, resulting in an ultrahigh energy density of 9681 mWh/g (referenced to the standard hydrogen electrode potential). This energy density represents the highest among all two-dimensional (2D) topological quantum anodes and surpasses that of most currently known 2D anode materials for Li-ion batteries. Furthermore, the formation of a vacancy in the BeN monolayer induces a unique "self-doping" effect that promotes high electronic conductivity. Additionally, the BeN monolayer exhibits a diffusion energy barrier of 0.30 eV for Li-ion migration, a small-scale area expansion of 0.96% during the process of lithiation, and excellent wettability with the contacted electrolytes.

DOI: 10.1103/PhysRevResearch.6.013028

I. INTRODUCTION

Li-ion batteries, as the most mature and extensively utilized energy storage technology, have gained widespread application across a range of sectors, including portable electronic devices, electric vehicles, and large-scale power plants [1–4]. To achieve the goal of fast-charging electric vehicle batteries to reach 80% pack capacity within 15 min by 2023, as proposed by the U.S. Advanced Battery Consortium [5], there is an urgent requirement for anode materials that exhibit both high ionic conductivity and high electrical conductivity.

Topological quantum materials possess substantial potential as anode materials owing to their inherent high electrical conductivity, which remains unimpaired by defects or impurities, surpassing the limitations of conventional ones [6]. Three-dimensional (3D) porous semimetallic materials represented by carbon [7–10], silicon [11], and boron [12] have already been investigated as anodes for Li- and Na-ion batteries. These materials exhibit excellent cycling stability; however, they have relatively low specific capacities ranging from 298 to 930 mAh/g for Li-ion batteries. This limitation hinders the miniaturization of equipment during the charging and discharging processes [13,14].

The exceptional mechanical strength, chemical stability, and high specific surface area exhibited by two-dimensional (2D) materials have garnered substantial research interest. Currently, substantial efforts are focused on the development of 2D topological quantum materials as anode materials for Li-ion batteries, aiming to enhance specific capacity and energy density. This family of 2D topological quantum materials contains graphene and its analogs [15–18] (e.g., borophene, silicene, germanene, and stanene), carbon-based materials [19–23] (e.g., C_4N, Si_3C, NbC, MnC, and SiC), boron-based materials [16,24–26] (e.g., B_3S, B_3P, BeB_2, MgB_2, and BP), and others [27] (e.g., FeSe). In general, 2D topological quantum materials exhibit improved specific capacity compared to 3D topological quantum materials, as seen in examples such as Si_3C (1394 mAh/g) [21], B_3S (1662 mAh/g) [24], and B_3P (1691 mAh/g) [25]. Furthermore, such materials showcase small-scale area expansion. However, their energy density remains lower than those of conventional 2D anode materials used in Li-ion batteries.

In this study, we designed a nodal-line semimetal anode material for Li-ion batteries that exhibits the highest energy density among all known 2D topological quantum materials and is comparable to conventional 2D anode materials. Using the swarm-intelligence structure search method and first-principles calculations, we focused on Be_xN_y monolayers and carried out an extensive computational study. We found a highly desired nodal-line semimetal anode BeN for Li-ion batteries. The BeN anode exhibits an impressive energy density of up to 9681 mWh/g, thanks to its high specific capacity reaching 3489 mAh/g and a low average open-circuit voltage (OCV) of 0.15 V. Additionally, the BeN anode exhibits several notable characteristics. Firstly, the BeN anode

*xml@calypso.cn
†jian_hao@jsnu.edu.cn

demonstrates a distinctive "self-doping" effect, effectively enhancing its electronic conductivity. Secondly, it exhibits a remarkably low diffusion energy barrier (0.30 eV) for Li atom migration on the BeN surface. Thirdly, it demonstrates excellent wettability with the electrolytes, ensuring robust interaction. Lastly, the area expansion of the BeN anode upon lithiation is as small as 0.96%.

II. CALCULATION METHODS

Structure searches for Be_xN_y $(0 < x/y \leqslant 1,\ 1 \leqslant y \leqslant 4)$ monolayers (involving four formula units at most) are performed using the CALYPSO method [28–31], which has been extensively used for structural predictions [32–35]. The local structural relaxations and electronic property calculations are performed based on the density functional theory [36] within the generalized gradient approximation [37] using the Vienna *ab initio* simulation package (VASP) [38]. The projector augmented-wave approximation [39] is adopted, treating $2s^2$ and $2s^2\,2p^3$ electrons as valence electrons for Be and N, respectively. The plane-wave cutoff energy of 550 eV and a dense Monkhorst-Pack grid spacing [40] of $2\pi \times 0.03\,\text{Å}^{-1}$ are adopted during the self-consistent calculation. The total energy and force convergence precisions are 10^{-5} eV and $0.01\,\text{eV}\,\text{Å}^{-1}$, respectively. It is important to clarify that the total energy referred to exclusively pertains to the electronic energy component, without the incorporation of vibrational contributions. The dynamic stability is investigated by the phonon calculations via the direct supercell method as implemented in the PHONOPY code [41,42]. The thermal stability of predicted structures is confirmed by *ab initio* molecular dynamics simulations (AIMD) with a total simulation time of 10 ps at 1fs intervals. The temperature is maintained at 300 K using the Nosé-Hoover chain thermostat [43]. The van der Waals correction is considered by the nonlocal optB86b-vdW density functional [44] during the calculations of adsorption energy. The climbing image nudged elastic band (NEB) method [45] is employed to locate the minimum-energy pathway between the given initial and final configurations, allowing the estimation of energy barriers for Li atom diffusion on the Be-N surfaces.

III. RESULTS AND DISCUSSION

A. Crystal structure and electronic properties of intrinsic and defective BeN monolayer

As shown in Fig. 1(a), we identified the BeN monolayer global minimum which adopts a monoclinic structure in $C2/m$ symmetry, with the lattice constants being $a = 16.75$ Å and $b = 3.00$ Å, Structure information can be found in Table SI in the Supplemental Material (SM) [46]. The monolayer of BeN is composed of two distinct types of hexagons: Be_2N_4

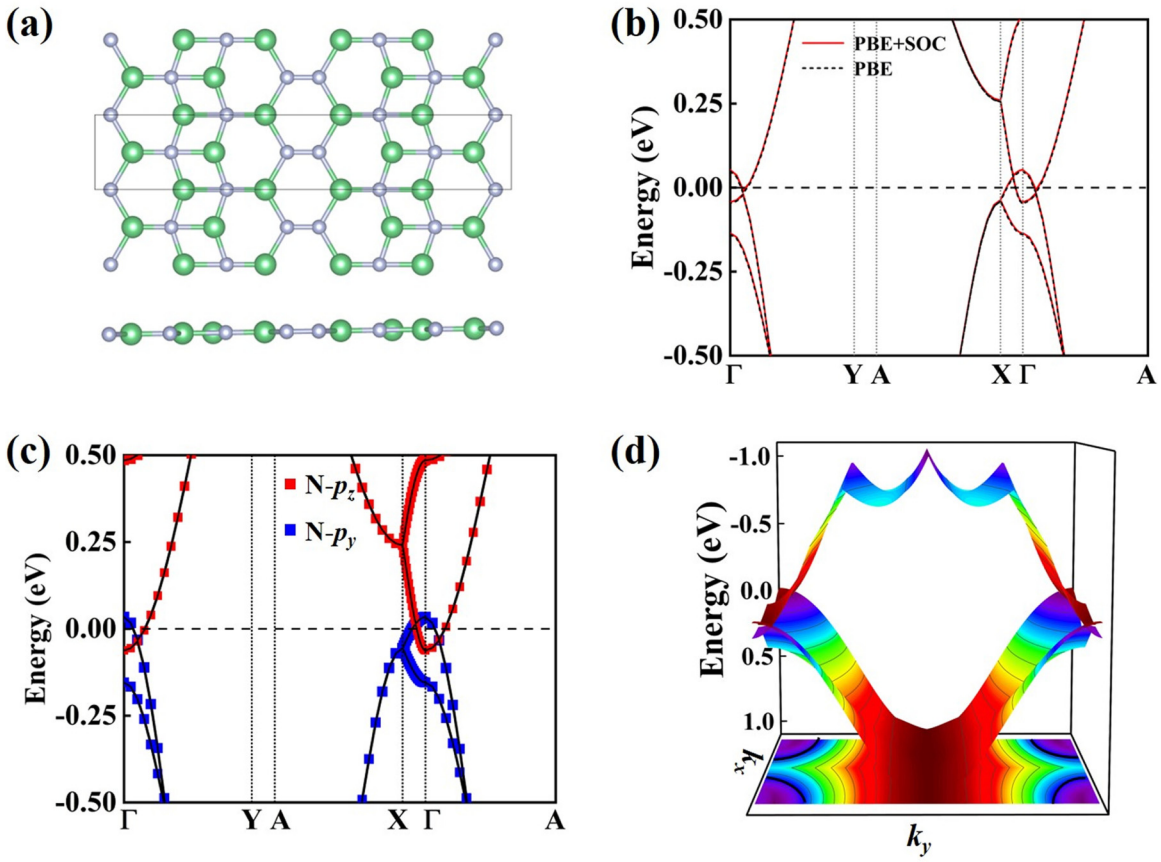

FIG. 1. (a) Top and side views of optimized BeN monolayer. (b) Band structures of BeN monolayer with and without the inclusion of the SOC effect. (c) Orbit-resolved band structure of BeN monolayer. (d) A three-dimensional band structure and projection showcasing a Dirac nodal line highlighted by black lines. The Fermi level is set to be zero.

and Be_3N_3. The N-N bond in BeN is double bonded with a bond length of 1.28 Å, which is slightly longer than that (1.21 Å) of a typical N = N bond in N_2F_2. The average length of the Be-N bond is 1.63 Å. The electron localization function calculations [47] of the BeN monolayer show the strong covalent interaction between the nearest-neighbor N atoms and between Be and N atoms because of obvious electron localization (Fig. S1(a) in the SM [46]). Bader charge analysis [48] further shows that each Be atom transfers 1.67 $|e|$ to the N atom (Table SII in the SM [46]). Therefore, the BeN monolayer exhibits the coexistence of covalent and ionic bonds.

The cohesive energy of BeN is −6.53 eV/atom with respect to the decomposition into the isolated Be and N atoms, indicating the possibility of being synthesized. The calculated phonon dispersion confirms that the BeN monolayer is dynamically stable as evidenced by the absence of imaginary frequencies in the entire Brillouin zone (Fig. S1(b) in the SM [46]). To assess the thermal stability of BeN monolayers, AIMD simulations have been performed at temperatures of 300 K with a time length of 10 ps (Fig. S1(c) in the SM [46]). The BeN monolayer can retain its structural integrity without obvious distortions, which is further confirmed by the small energy fluctuation. The elastic constants of BeN have been calculated and presented in Table SIII in the SM [46], which meet the Born criteria [49] for 2D systems, indicating its mechanical stability.

Figures 1(b) and 1(c) show the band structures of the BeN monolayer. The band structure remains nearly unchanged with the inclusion of the spin-orbit coupling (SOC) effect, revealing the weak SOC effect in the BeN monolayer. Consequently, for subsequent calculations, the SOC effect is disregarded. The band structure of BeN exhibits evident metallic characteristics, featuring a holelike band attributed to the N$-p_y$ orbital and an electronlike band originating from the N$-p_z$ orbital intersecting near the Fermi level. Importantly, all these bands exhibit double degeneracy, indicating the presence of fourfold Dirac fermions at the gapless nodes. In Fig. 1(d), the 3D band structure of the BeN monolayer is illustrated. Notably, the BeN monolayer exhibits a distinctive nodal loop, which is highlighted by black lines.

We investigated the effect of lattice vacancy in the BeN monolayer on its electronic properties. We removed a Be or a N atom from a $1 \times 3 \times 1$ supercell (initially containing 24 Be and 24 N atoms) to create the vacancies, yielding a vacancy concentration of approximately 2.1%. After optimizing the structure, our findings reveal that the introduction of two Be vacancies [Figs. 2(a) and 2(b)] and one N vacancy in the Be3N3 hexagon [Fig. 2(d)] does not significantly alter the local atomic reconstruction. In contrast, the N vacancy in the Be_2N_4 hexagon exhibits a relatively substantial impact on the local atomic reconstruction, as illustrated in Fig. 2(c). The calculated formation energies for BeI and BeII vacancies are 8.17 and 9.09 eV, respectively, which are lower than those of NI and NII vacancies (9.52 and 11.50 eV, respectively). This result indicates that the formation of a Be vacancy is comparatively more facile. We also conducted NEB calculations to gain insights into the kinetics processes. Results reveal that the energy barriers for BeI, BeII, and NI vacancies are 8.1, 9.1, and 9.4 eV, respectively (Fig. S2 in the SM [46]). These results indicate that the formation of a BeI vacancy is relatively favorable, suggesting its relative ease of formation.

The electronic band structures, as depicted in Figs. 2(e), 2(f), and 2(h), indicate that the characteristic nodal-line feature observed in the pristine BeN monolayer is likely to persist even in the presence of vacancies. The presence of distinct types of vacancies in a material can act as sources of self-doping, subsequently influencing its electrical conductivity. Depending on the material's intrinsic properties and the particular type of vacancy, self-doping can manifest as either *n* type or *p* type, thereby increasing electron or hole conductivity, respectively. Our calculations of formation energy and NEB analysis indicate that the BeI vacancy is more likely to form, leading to *n*-type self-doping and, consequently, enhancing the material's electron conductivity. The formation of vacancy defects inducing a distinctive "self-doping" effect has been observed in B_2S [50] and Be_2C_5 [51] Dirac anode materials.

B. Li- and Na-ion adsorption and diffusion on the BeN anode

The adsorption and migration of Li and Na ions in the BeN monolayer are crucial in determining the suitability of 2D materials as anodes. Here, we consider ten possible adsorption sites with high geometric symmetry (Fig. S3(a) in the SM [46]). These sites are further categorized into three distinct types: hollow (H), top (T), and bridge (B). While simulating the adsorption and diffusion of metal atoms on the BeN monolayer, a $1 \times 3 \times 1$ supercell is used to prevent the interaction between the adjacent metal atoms. After structural relaxation, we find only three possible adsorption sites, namely the H1, H2, and B1 sites. The results of adsorption energy calculations are summarized in Fig. 3(a) and Table SIV in the SM [46]. The adsorption energies of Li and Na ions on these sites are negative, ranging from −1.22 to −0.36 eV and −1.06 to −0.48 eV, respectively. Such negative values are significant enough to hinder the formation of metallic dendrites. For both Li and Na atoms, the H1 site is the optimum adsorption one. It is imperative to acknowledge that dendrite formation is a multifaceted process influenced by a wide array of factors [52]. These factors encompass not only thermodynamic considerations but also kinetic parameters, such as the ion diffusion coefficient, charge-transfer coefficient, current density, ion mobility, and more. The more negative surface energy and lower migration energy do indeed indicate that, from an energetic standpoint, Li dendrites are not inherently more prone to form. Consequently, it is essential to recognize that a comprehensive understanding of dendrite formation cannot be limited solely to the analysis of adsorption energy.

The adsorption mechanism is analyzed from two aspects: charge transfer and orbital hybridization. In the inset of Fig. 3(a), it is observed that the length of the Li/Na-N1 bond is 2.07/2.46 Å, which is smaller compared to the Li/Na-N2 bond length (2.55/2.94 Å). This difference leads to a stronger orbital hybridization between Li/Na and N1 atoms, evident in the clear overlap between the N1-*p* and Li/Na-*p* orbitals situated below the Fermi level [as depicted in Figs. 3(b) and 3(c)]. Bader charge analysis results reveal that upon adsorption of Li (Na) ions on the BeN surface, the N2 atom gains 0.13 (0.10) $|e|$, which is greater than the gain in charge by the N1 atom

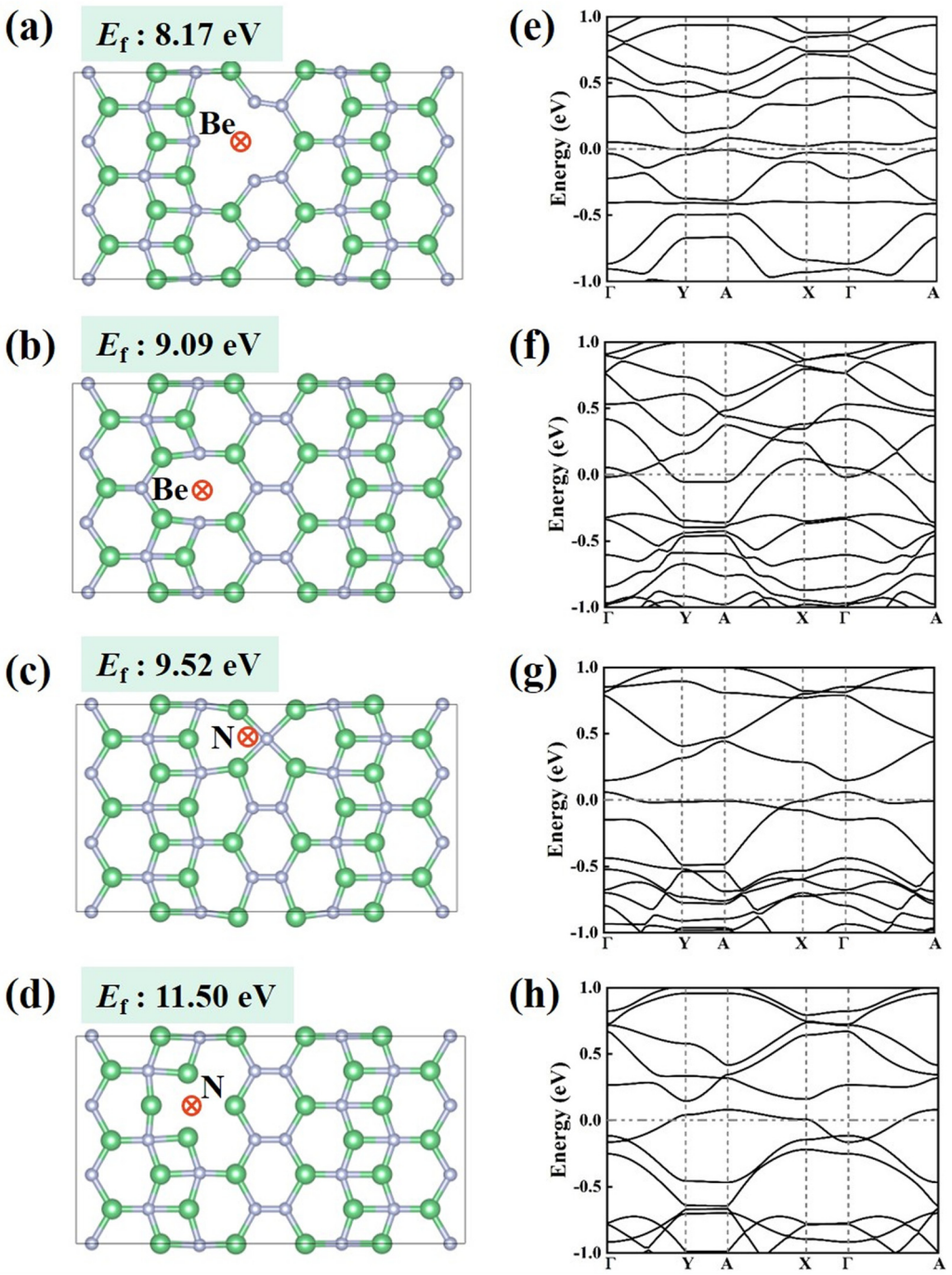

FIG. 2. The relaxed structures of the 1 × 3 BeN supercell with various vacancies, including (a) BeI vacancy, (b) BeII vacancy, (c) NI vacancy, and (d) NII vacancy. The corresponding electronic band structures are presented in (e)–(h) for each vacancy configuration.

[0.06 (0.03) $|e|$]. Therefore, both electron transfer (especially between Li/Na and N2) and orbital hybridization (particularly between Li/Na and N1), play a crucial role in the adsorption of Li/Na on the BeN surface. The adsorption of a Li/Na atom preserves the metallicity of the BeN monolayer (Figs. S3(b) and S3(c) in the SM [46]).

We have chosen three distinct diffusion pathways [paths 1–3, as depicted in Fig. 4(a)] to evaluate the diffusion energy barrier and assess the mobility of Li/Na ions. Among these pathways, path 2 stands out, revealing the lowest diffusion energy barrier for both Li and Na atom migration, estimated at 0.30 and 0.11 eV, respectively. These values are comparable to most 2D anodes [Table I], such as B_3P [25] (0.37 eV for Li), SiC [20] (0.57 eV), B_3S [24] (0.40 eV), BGe [53] (0.2 eV for Na) and BP [54] (0.16 eV for Na). In practical scenarios, the energy barrier for the migration of Li and Na atoms is expected to increase significantly, especially when considering multilayer BeN as anode materials. We have conducted calculations to determine the diffusion barrier for Li atom migration between the layers of bilayer BeN. The diffusion energy required for Li atom migration between the layers of bilayer BeN is 0.52 eV, higher than that of the corresponding

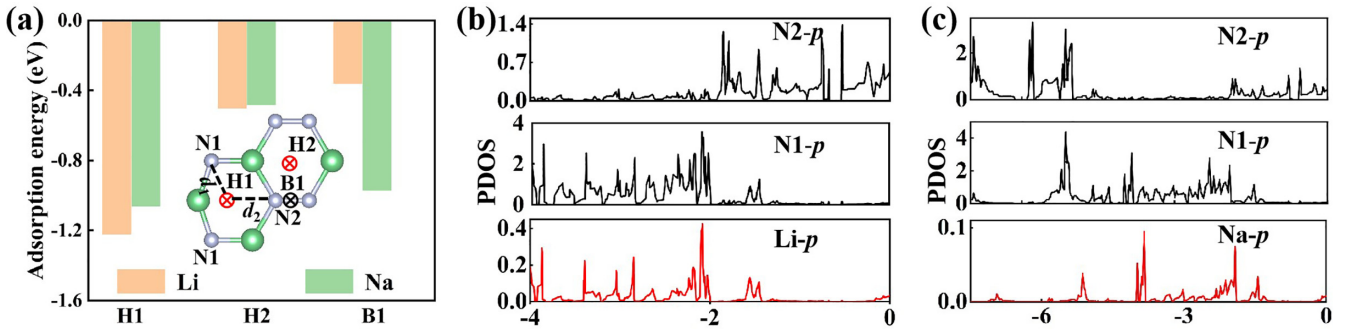

FIG. 3. (a) Adsorption energies of Li and Na atoms at different stable adsorption sites of BeN monolayer. The inset showcases the adsorption sites, and Li/Na-N bond length (d_1, d_2). PDOS for (b) Li and (c) Na adsorbed at the H1 site of BeN monolayer.

BeN monolayer (Fig. S4 in the SM [46]). Nevertheless, it is noteworthy that the optimal diffusion pathway remains consistent.

C. Specific capacity, average OCV, energy density, and durability

The maximum specific capacity can be determined when the adsorption energy becomes positive or converges with increasing Li/Na ion concentrations. The layer-by-layer average adsorption energy (E_{ave}) has been calculated to examine the Li/Na atoms' storage performance of the BeN monolayer. The adsorption energy decreases as the number of Li/Na atoms increases due to repulsion forces between neighboring atoms (Fig. 4(d) and Fig. S5(a) in the SM [46]). The theoretical specific capacity of anode materials is proportional to the number of adsorption atoms. Thus, the relationship between the adsorption concentration and behavior of Li/Na atoms on the BeN monolayer can be studied by adsorbing multiple Li/Na atoms on both sides of BeN. Calculated results demonstrate that a maximum of 72 Li atoms can be accommodated on both sides of the BeN monolayer, i.e., a total of two layers with 18 atoms per layer on one side, and the corresponding stoichiometric ratio is $BeNLi_3$. As a result, the theoretical specific capacity is calculated to be as high as 3489 mAh/g, which is very high among the reported 2D topological materials and higher than those of most 2D representative materials (Table I and Fig. S6 in the SM [46]). AIMD simulations at 300 K for 10 ps demonstrate that the BeN monolayer is slightly distorted when multiple Li atoms are

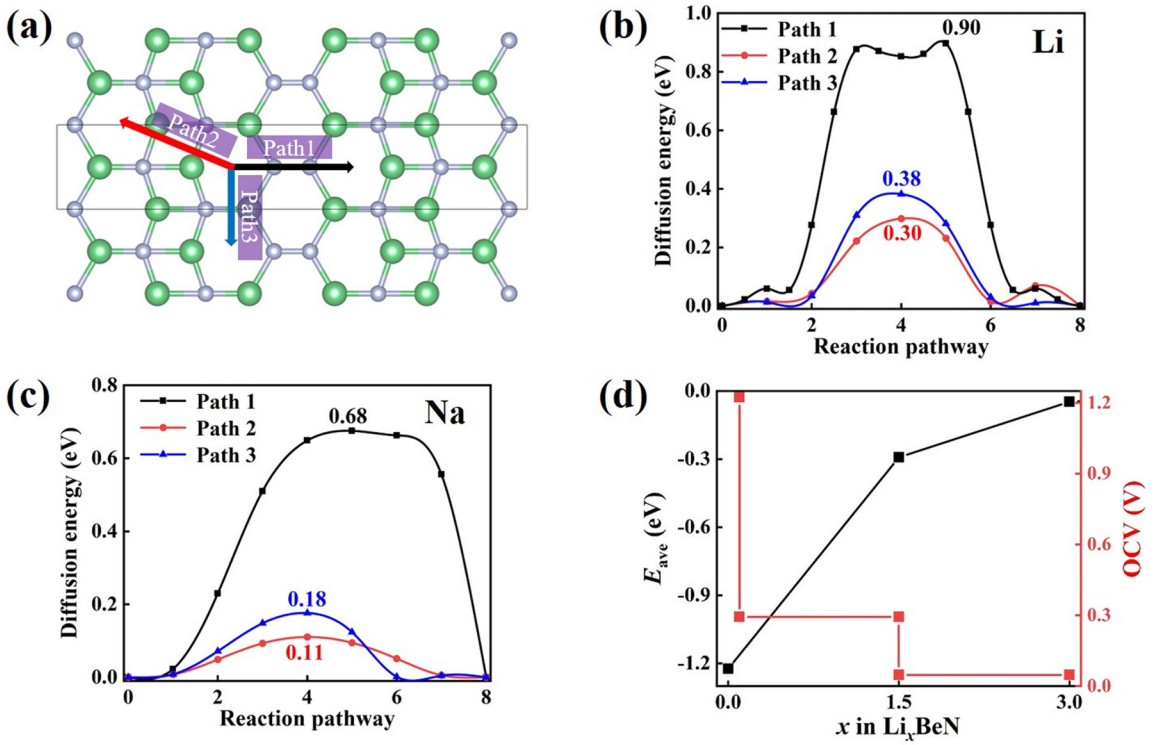

FIG. 4. (a) Alkali metal ions diffusion pathways on the BeN surface. (b) and (c) refer to the diffusion energy barriers associated with the migration of Li and Na ions, respectively. (d) Calculated OCV and average adsorption energy (E_{ave}) of Li-ion on BeN monolayer as the number of adsorbed metal atoms (x) increases.

TABLE I. Comparative summary of the diffusion barrier energy (eV), open-circuit voltage (OCV, V), specific capacity (mAh/g), energy density (mWh/g), and area expansion of different anode materials for Li-ion batteries. The energy density is calculated using specific capacity and OCV in original reports.

	Anode	Barrier energy (eV)	OCV (V)	Specific capacity (mAh/g)	Energy density (mWh/g)	Area expansion	Refs.
Topological quantum 2D materials	BeN	0.3	0.15	3489	9681	0.96%	
	C_4N	0.21	0.11	2158	5093		[58]
	B_3S	0.4	0.16	1662	4786		[24]
	Si_3C	0.46	0.20	1675	4757	0.3%	[21]
	BeB_2	0.47	0.33	1750	4742		[26]
	MgB_2	0.61	0.70	1750	4095		[26]
	B_3P	0.37	0.65	1691	4041		[25]
	BP	0.19	0.17	1282	3679	1.52%	[59]
	NbC	0.2	0.27	1021	2828		[22]
	Θ-graphene	0.35	0.3	876	2400		[17]
	MnC	0.15	0.15	800	2312		[22]
	*h*567	0.35	0.3	697	1910		[18]
	FeSe	0.16	0.25	658	1836	3.9%	[27]
	SiC	0.57	0.11	501	1468	1.49%	[20]
	Borophene	0.27	0.43	504	1315	2.5%	[60]
	Silicene	1.2	/	954	/		[15]
	Stanene	0.1	/	226	/		[15]
	Germanene	/	/	369	/		[15]
Typical 2D materials	Mg_4B_6	/	0.32	4299	11211	1.95%	[61]
	B_7P_2	0.59	0.24	3117	8728		[23]
	SiP_3	0.11	0.19	2658	7575		[62]
	BGe	0.2	0.33	1927	5222		[53]
	BN_2	0.05	0.61	2071	5032		[63]
	NiC_3	0.5	0.15	1698	4907		[64]
	Be_2C	0.11	0.33	1785	4837		[65]
	BeP_2	0.15	0.17	1510	4333		[66]
	FeC	0.26	0.37	1579	4216		[67]
	BSi	0.37	0.53	1378	3459		[68]
	AsP	0.17	0.17	1011	2901	6.9%	[57]
	GaN	0.079	0.26	938	2608		[69]
	Mn_2C	0.024	0.15	887	2563		[70]
	BC_3	0.04	0.48	883	2260		[71]
	B_2N	1.38	1.07	1082	2131	1.1%	[72]
	PC_6	0.33	0.23	717	2014		[73]
	Ca_2C	0.027	0.1	582	1711		[74]
	Mo_2C	0.035	0.14	526	1525	0.4%	[75]
	TaB	0.09	0.54	559	1398		[76]
	BAs	0.52	0.49	522	1331		[77]
	GaS	0.11	0.53	526	1320		[78]
	Sc_2C	0.018	0.27	462	1279		[79]
	PtN_2	0.25	0.44	480	1248		[80]
	AlC	0.78	1.38	739	1227	6.46%	[81]
	Ti_2N	0.017	0.53	487	1222		[82]
	C_3N	0.41	0.15	383	1107		[83,84]
	VS_2	0.22	0.93	466	983		[85]
	YS_2	0.33	0.38	350	931		[86]

adsorbed [Fig. 5(a)]. After the removal of all Li atoms from the BeN surface, we rerun the AIMD simulations and find that the slightly deformed BeN monolayer can quickly recover its initial configuration [Fig. 5(b)]. These results reveal the good phase stability of the BeN monolayer during the Li atoms' insertion/extraction processes. The maximum adsorption Na concentration corresponds to BeNNa, in which the BeN monolayer adsorbs a total of 26 atoms on both sides. After being fully optimized, the adsorption of Na atoms will cause structural deformation of the BeN monolayer (Fig. S5(b) in the SM [46]). Therefore, the BeN monolayer is not suitable as an anode for Na-ion batteries. Thus, we calculate the average OCV, energy density, and area change of the BeN monolayer as an anode for Li-ion batteries.

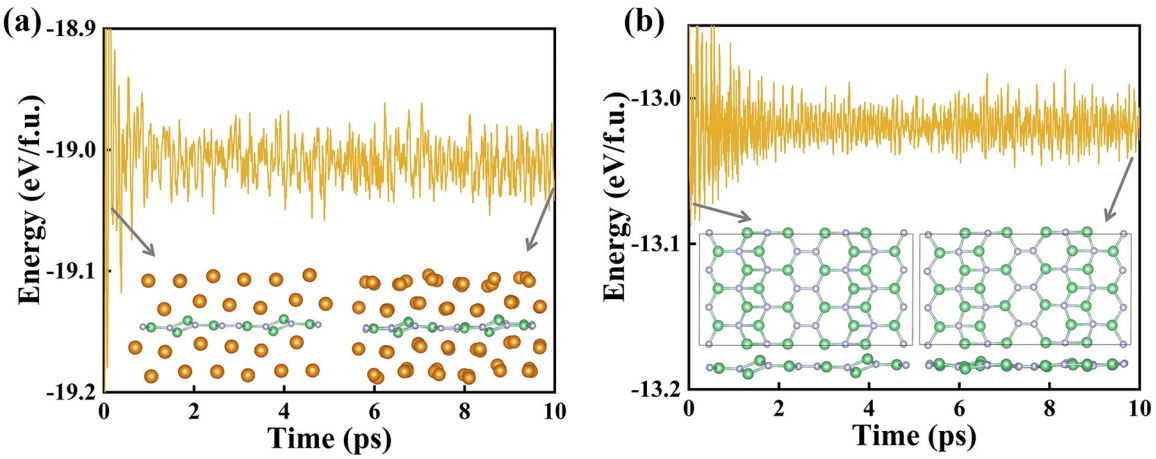

FIG. 5. The energy evolution of (a) $BeNLi_3$ and (b) BeN monolayer obtained after removing all adsorbed Li atoms during AIMD simulations at 300 K.

Two stable $BeNLi_x$ ($x = 1.5$ and 3) structures are considered to compute the average OCV, and calculated results show that the average OCV value of BeN for Li storage versus the metal electrode is computed to be 0.15 V, comparable to many 2D materials (Table I). Energy density is a pivotal parameter for assessing the electrochemical performance of anode materials in industrial applications. The standard hydrogen electrode potential (SHE) is used as the universal cathode reference potential in these evaluations [55]. The energy density D can be estimated using the equation of $D = |–3.04\,\mathrm{V} + V_{\mathrm{ave}}| \times C$ [55], which takes into account the average OCV denoted as V_{ave}, the specific capacity denoted as C, and the relative potential for Li. The energy density of the BeN anode is calculated to be 9681 mWh/g, which is the highest among 2D topological anode materials and higher than those of most 2D representative materials (Table I and Fig. S6 in the SM [46]). This impressive value indicates that BeN has great potential for storing a substantial amount of energy in Li-ion batteries.

In a practical electrochemical energy storage device, an isolated BeN layer is not a realistic configuration. The presence of other BeN layers in atomic proximity can significantly influence the adsorption and intercalation energetics, thereby playing a pivotal role in the overall behavior and performance of the system. Therefore, it may be more realistic that a $(1 \times 3 \times 1)$ BeN monolayer can accommodate up to 18 Li atoms on each side. Thus, the specific capacity is reduced by half and the energy density is decreased to 5824 mWh/g. Even so, the value is still higher than those of most 2D representative materials (Table I and Fig. S6 [46]).

The computed area expansion for $BeNLi_3$ is only 0.96%. This minimal fluctuation neither leads to electrode fracture nor induces any specific capacity degradation. To achieve a more accurate estimation of the volume expansion of BeN, we have constructed a model based on the AA-stacking bilayered BeN structure, as illustrated in Fig. S7 [46]. Following complete structural optimization, the interlayer spacing of the AA-stacking BeN is 3.56 Å. Upon adsorbing a single layer of Li atoms, precisely 18 Li atoms situated between two $(1 \times 3 \times 1)$ BeN monolayers, the interlayer spacing expands to 3.75 Å. Consequently, the calculated volume expansion of the BeN anode amounts to approximately 5.3%, a value notably smaller than that of graphite anode material (12%) [56] and AsP (6.9%) [57].

D. Wettability of typical solvent molecules and metal salts in the BeN surface

The wettability of the BeN anode by typical solvent molecules is a crucial factor for assessing the overall performance and stability of the battery system [87]. To evaluate the compatibility of solvent molecules with the BeN surface, we selected diethyl carbonate (DEC), dimethyl carbonate (DMC), ethylene carbonate (EC), and propylene carbonate (PC) as the solvents. Several adsorption sites for the solvent molecules on the BeN surface were tested to identify the most energetically favorable configuration (Fig. S8 in the SM [46]). In Table II, it is shown that the calculated adsorption energy of all the considered solvent molecules displays negative values, ranging from −0.46 to −0.66 eV. These negative values indicate a strong interaction between the solvent molecules and the BeN surface. Notably, the adsorption energies of solvent molecules on BeN are comparable to those on graphene [50] (−0.54 to −0.87) and B_2S [50] (−0.44 to −0.69), suggesting an excellent wettability of BeN and a favorable wetting process.

We also studied the wettability of metal salts on the BeN surface, such as $LiClO_4$, LiFSI, $LiPF_6$, and LiTFSI. The most energetic configurations of metal salt absorbed on the BeN surface are illustrated in Fig. S9 in the SM [46]. The calculated

TABLE II. Comparison of adsorption energies of solvent molecules DEC, DMC, EC, and PC on BeN, graphene, and B_2S anodes.

	E_{ad} (eV)		
Solvent molecule	BeN	Graphene	B_2S
DEC	−0.46	−0.87	−0.69
DMC	−0.56	−0.54	−0.44
EC	−0.66	−0.56	−0.51
PC	−0.48	−0.69	−0.63

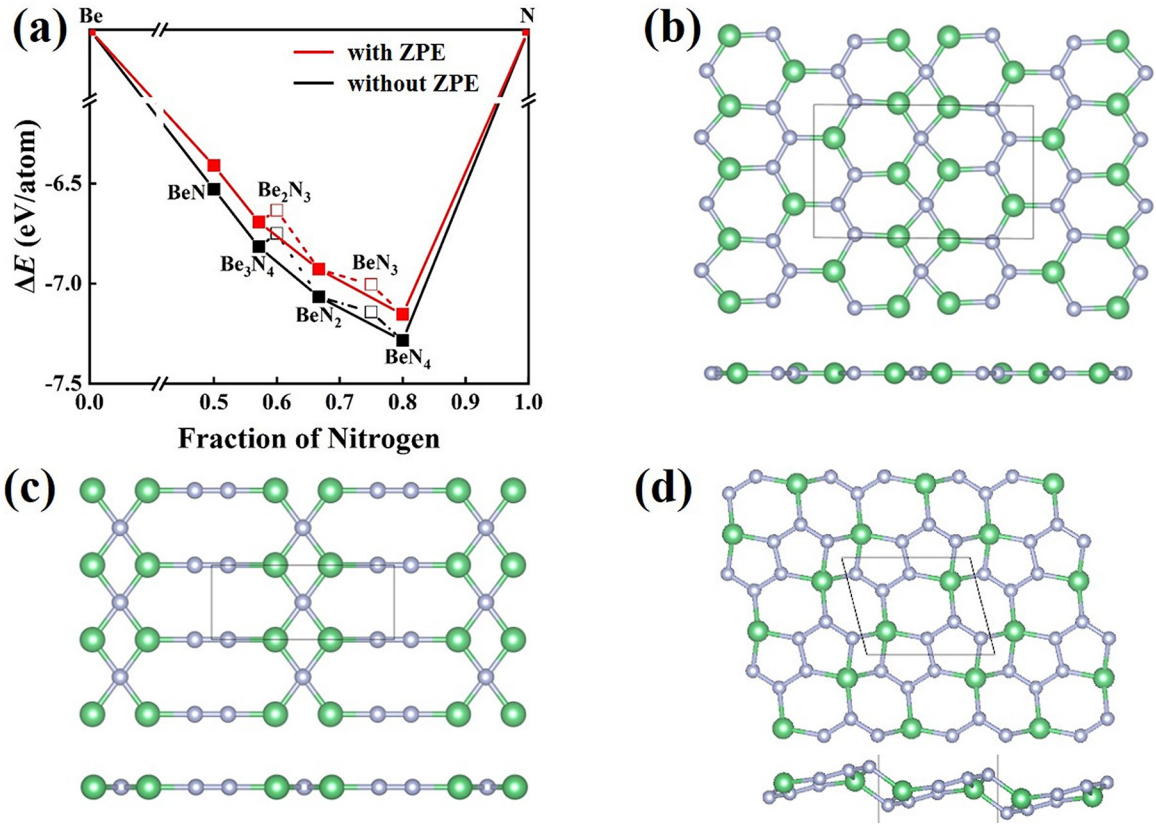

FIG. 6. (a) Convex hull diagram for the Be-N system based on the formation energies concerning decomposition into the isolated Be and N atoms with and without the inclusion of zero-point energy (ZPE). The stable and metastable phases are marked by solid and hollow blocks, respectively. The crystal structures of (b) Be_3N_4, (c) Be_2N_3, and (d) BeN_3 monolayers.

adsorption energy of all the considered metal salts displays negative values, ranging from −0.46 to −1.29 eV. Therefore, a stable solid electrolyte interphase (SEI) layer could be formed at anode surfaces. In addition, the calculated work function of BeN is 4.60 eV, comparable to that of graphene (4.63 eV) and B_2S (4.57 eV) [50], indicating its stability when in contact with electrolytes. Nonetheless, it is imperative to stress that due to the exceptionally high energy density of BeN, a comprehensive understanding and controlling of the formation of the SEI layer is of utmost significance. Therefore, strategies for optimizing SEI formation and stability include choosing appropriate electrolyte compositions, additives, and electrode materials, as well as doing partial cycling or applying another structural modification to the system can promote the development of a robust and protective SEI.

E. Crystal structures, electronic properties, and potential as anode materials of Be_3N_4, Be_2N_3, and BeN_3 monolayers

We successfully predicted the experimentally synthesized BeN_4 [88,89] and theoretically proposed BeN_2 monolayers [90–94] using the CALYPSO method, indicating the reliability of the methodology. Additionally, three other 2D Be-N compounds with the stoichiometries Be_2N_3, Be_3N_4, and BeN_3 have been predicted. Note that the new predicted BeN_3 monolayer is energetically more favorable than the previously proposed structure [95] by 0.31 eV/f.u. The convex hull diagram for the Be-N system based on the formation energies (Table SV in the SM [46]) concerning isolated Be and N atoms is shown in Fig. 6(a). One can see that in addition to BeN, our study identified a thermodynamically stable Be_3N_4 and two metastable BeN_3, and Be_2N_3, as shown in Figs. 6(c) and 6(d).

Through phonon spectra calculations and AIMD simulations, we have confirmed their dynamic and thermal stability, respectively, as depicted in Fig. S10 in the SM [46]. Be_3N_4 and BeN_3 are semiconductors with band gaps of 0.06 and 0.74 eV, respectively, and Be_2N_3 exhibits metallic properties (Fig. S11 in the SM [46]). Given that both Be_3N_4 and B_2N_3 possess flat structures, which facilitate the smooth movement of metal ions, we conducted further assessments of their potential as anodes for Li-ion batteries. Our findings indicate that only Be_3N_4 shows promise as an anode material for Li-ion batteries. In particular, Be_3N_4 exhibits a specific capacity of 1129 mAh/g (refer to $Be_3N_4Li_{3.5}$) and features a diffusion energy barrier of 0.22 eV (Fig. 7).

IV. CONCLUSIONS

In summary, our study extensively explores the Be-N system through a combination of the CALYPSO method and first-principles calculations. We have successfully identified a nodal-line semimetal, BeN, as a highly promising anode material for Li-ion batteries, boasting an extraordinary ultrahigh energy density of 9681 mWh/g. This remarkable performance is attributed to its substantial specific capacity of 3489 mAh/g and a relatively low average OCV of

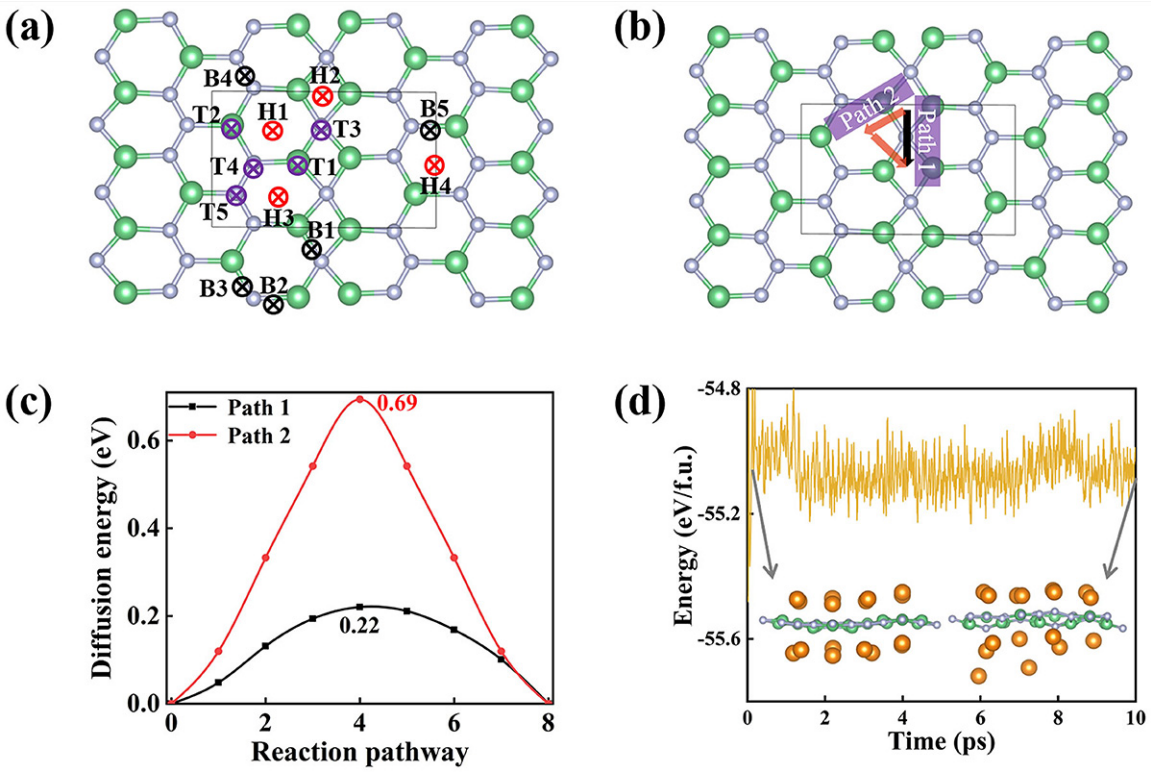

FIG. 7. (a) Possible adsorption sites in the Be_3N_4 monolayer. (b) Li atoms diffusion pathways on Be_3N_4. (c) Corresponding diffusion energy barrier for Li atom on Be_3N_4. (d) Evolution of energy of $Be_3N_4Li_4$ during AIMD simulations at 300 K. The insets are the images of structures at the beginning and end of the 10 ps simulation.

0.15 V. Significantly, this energy density value surpasses that of the most currently known 2D Li-ion battery anode materials. The BeN monolayer exhibits outstanding electronic conductivity and possesses a unique "self-doping" effect arising from the formation of Be or N vacancies. Additionally, the BeN anode demonstrates several other desirable characteristics. It presents an energy barrier of 0.30 eV for rapid Li-ion migration, exhibits robust wettability with solvent molecules, maintains good phase stability during Li-ion insertion/extraction processes, and experiences only a minor 0.96% area expansion during lithiation. These qualities collectively establish the BeN monolayer as a promising candidate for nodal-line semimetal anodes in Li-ion batteries.

ACKNOWLEDGMENTS

The authors acknowledge funding support from the National Natural Science Foundation of China (Grants No. 12374010, No. 12074154, No. 11904142, and No. 11722433), Six Talent Peaks Project, and 333 High-Level Talents Project of Jiangsu Province. The computational resources have been provided by the High-Performance Computing Center of the School of Physics and Electronic Engineering of Jiangsu Normal University.

APPENDIX A: COMPUTATIONAL DETAILS

The cohesive energy (E_{coh}) is a useful parameter to evaluate the possible synthesis of the Be_xN_y monolayer, which is calculated according to the following equation:

$$E_{coh} = (E_{Be_xN_y} - yE_N - xE_{Be})/(x + y),$$

where $E_{Be_xN_y}$, E_N, and E_{Be} are the total energies of the Be_xN_y monolayer, isolated N atom and Be atom, respectively. x, and y are the number of Be and N atoms, respectively.

The formation energy of a defect (E_f), determining the possibility of its existence in BeN, can be calculated by

$$E_f = E_{defect} + E_{Be/N} - E_{BeN},$$

where E_{defect} and E_{BeN} are the total energies of the defective and intrinsic BeN monolayer, respectively. Also, $E_{Be/N}$ represents the energy of an isolated Be/N atom.

The adsorption energy (E_{ad}), for the metal atom on Be_xN_y monolayer is calculated as follows:

$$E_{ad} = E_{Be_xN_yM} - E_{Be_xN_y} - \mu_M,$$

where $E_{Be_xN_yM}$ and $E_{Be_xN_y}$ are the total energies of metal-loaded Be_xN_y and intrinsic Be_xN_y, respectively; μ_M is the chemical potential of Li/Na in their bulk states.

Similarly, the adsorption energy ($E_{ad\text{-}mol}$), for the solvent molecules and metal salts on the BeN monolayer is calculated as follows:

$$E_{ad\text{-}mol} = E_{BeNZ} - E_{BeN} - \mu_z,$$

where E_{BeNZ} and E_{BeN} are the total energies of solvent molecules absorbed on the BeN monolayer and intrinsic BeN, respectively, and μ_Z is the energy of isolated solvent molecules or metal salts.

The layer-layer average adsorption energy (E_{ave}) is defined as

$$E_{ave} = \frac{E_{all\text{-}Be_xN_y} - E_{(a-1)-Be_xN_y} - x\mu_{Li/Na}}{x},$$

where a represents the number of adsorbed Li/Na-ion layers, $E_{all\text{-}Be_xN_y}$ and $E_{(a-1)\text{-}Be_xN_y}$ are the total energies of Be_xN_y electrode with a and $(a-1)$ layer(s) of adsorbed Li/Na atoms, respectively; $\mu_{Li/Na}$ is the chemical potential of the Li/Na atom in bulk; and x refers to the largest number of adsorbed Li/Na atoms in one layer (on both sides).

The theoretical specific capacity (C) is evaluated by

$$C = \frac{zx_{max}F}{M_{Be_xN_y}},$$

where z is the number of valence electrons ($z = 1$ for Li/Na), x_{max} is the maximum number of adsorbed Li/Na atoms, F is the Faraday constant (26 801 mAh/mol), and $M_{Be_xN_y}$ is the molar mass of the Be_xN_y monolayer.

The average open-circuit voltage (V_{ave}) is roughly evaluated by

$$V_{ave} \approx -\frac{E_{ave}}{xe},$$

where E_{ave} and x are the layer-layer average adsorption energy and the largest number of adsorbed Li/Na atoms in one layer (on both sides), respectively.

Applying the Nernst equation, we can determine the electromotive force, denoted as OCP, as follows

$$\mathrm{OCP} = G/nF.$$

In this equation, G stands for the Gibbs free energy, n represents the equivalents of reactants converted into products per mole, and F is the Faraday constant. Notably, "nF" denotes the quantity of electricity passing through the cell, measured in coulombs. Thus, the average open-circuit voltage and OCP are found to be equivalent.

The area expansion (ε) for the BeN monolayer during the insertion of adatoms can be defined as

$$\varepsilon = \frac{A - A_0}{A_0},$$

where A_0 and A are the area of BeN and the area of the largest number of Li/Na atoms absorbed on BeN, respectively.

APPENDIX B: POTENTIAL OF Be_3N_4 AS ANODES FOR Li-ION BATTERIES

For the Be_3N_4 monolayer, 14 adsorption sites based on structural symmetry have been selected [Fig. 7(a)]. As shown in Table S3 in the SM [46], the Li atom tends to adsorb at the H2 and H1 sites, with the adsorption energy of −0.95 and −0.91 eV, respectively. We have chosen two diffusion pathways [paths 1 and 2, as depicted in Fig. 7(b)] to assess the mobility of Li ions. The lowest diffusion energy barrier for the Li atom is 0.22 eV along path 2 [Fig. 7(c)]. The maximum adsorption Li concentration corresponds to $Be_3N_4Li_4$, in which the Be_3N_4 monolayer adsorbs one-layer Li atoms on both sides. AIMD simulations at 300 K for 10 ps demonstrate that the Be_3N_4 monolayer is distorted when multiple Li atoms are adsorbed, and two Li atoms tend to escape after 10 ps [Fig. 7(d)]. Therefore, the calculated theoretical capacity is

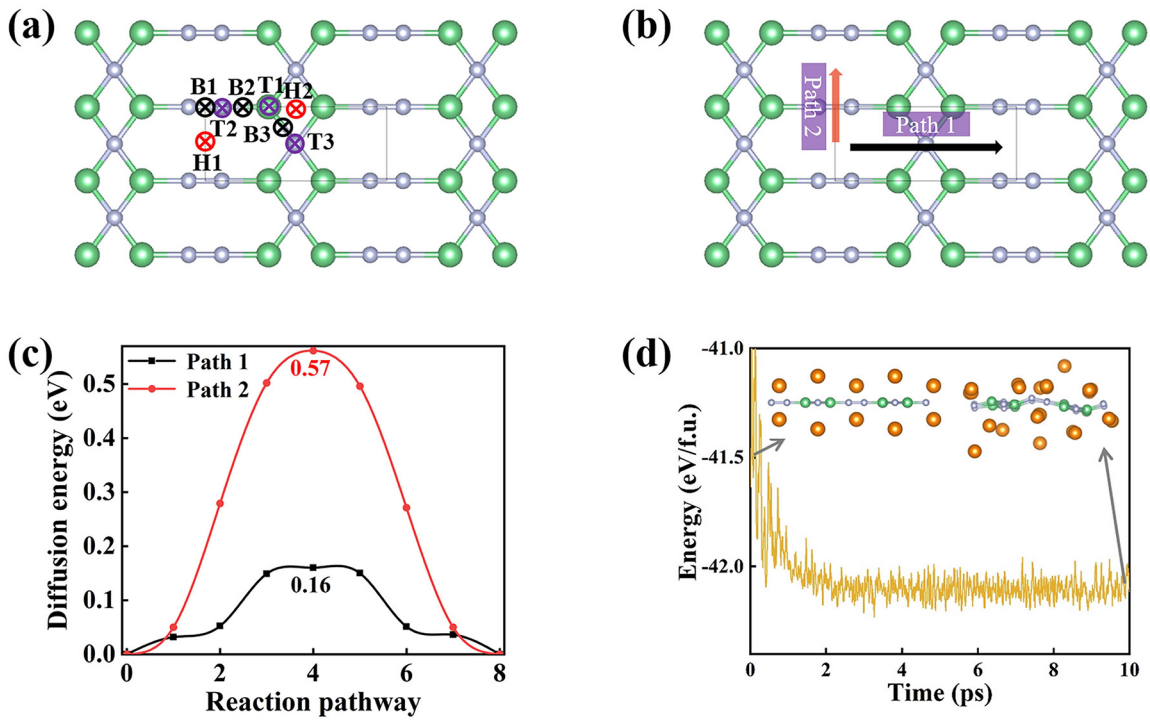

FIG. 8. (a) Eight possible adsorption sites in the Be_2N_3 monolayer. (b) Li atoms diffusion pathways on the Be_2N_3 surface. (c) Diffusion pathways and the corresponding diffusion energy barrier. (d) Evolution of energy of $Be_2N_3Li_4$ during MD simulations at 300 K. The insets are the images of structures at the beginning and end of the 10 ps simulation.

1129 mAh/g for $Be_3N_4Li_{3.5}$. Although the value is smaller than that of the BeN monolayer, it is still higher than those of most 2D materials, such as borophene, silicene, etc. (Table I).

APPENDIX C: Be_2N_3 IS NOT SUITABLE ANODES FOR Li-ION BATTERIES

As shown in Fig. 8, for the Be_2C_3 monolayer, eight potential adsorption sites are considered, and the Li atom ultimately only adsorbs at the center of the ring, with the lowest adsorption energy of −0.39 eV at the H1 site. We explored two possible paths for Li atom migration, and the lowest diffusion energy barrier for the Li atom is 0.16 eV. The maximum adsorption Li concentration corresponds to $Be_2N_3Li_4$, in which the Be_2N_3 monolayer adsorbs one-layer Li atoms on both sides. However, AIMD simulations have confirmed that $Be_2N_3Li_4$ undergoes folding at 300 K after 10 ps. Therefore, Be_2N_3 is not suitable as an anode for Li-ion batteries.

[1] J. Zhou, Q. Shi, S. Ullah, X. Yang, A. Bachmatiuk, R. Yang, and M. H. Rummeli, Phosphorus-based composites as anode materials for advanced alkali metal ion batteries, Adv. Funct. Mater. **30**, 2004648 (2020).

[2] D. Larcher and J.-M. Tarascon, Towards greener and more sustainable batteries for electrical energy storage, Nat. Chem. **7**, 19 (2015).

[3] N. Nitta, F. Wu, J. T. Lee, and G. Yushin, Li-ion battery materials: present and future, Mater. Today **18**, 252 (2015).

[4] B. Dunn, H. Kamath, and J.-M. Tarascon, Electrical energy storage for the grid: A battery of choices, Science **334**, 928 (2011).

[5] Y. Liu, Y. Zhu, and Y. Cui, Challenges and opportunities towards fast-charging battery materials, Nat. Energy **4**, 540 (2019).

[6] M. M. Obeid and Q. Sun, Recent advances in topological quantum anode materials for metal-ion batteries, J. Power Sources **540**, 231655 (2022).

[7] J. Liu, S. Wang, Y. Qie, C. Zhang, and Q. Sun, High-pressure-assisted design of porous topological semimetal carbon for Li-ion battery anode with high-rate performance, Phys. Rev. Mater. **2**, 025403 (2018).

[8] H. Xie, Y. Qie, M. Imran, and Q. Sun, Topological semimetal porous carbon as a high-performance anode for Li-ion batteries, J. Mater. Chem. A **7**, 14253 (2019).

[9] Y. Qie, J. Liu, S. Wang, Q. Sun, and P. Jena, Tetragonal C_{24}: A topological nodal-surface semimetal with potential as an anode material for sodium ion batteries, J. Mater. Chem. A **7**, 5733 (2019).

[10] J. Liu, S. Wang, and Q. Sun, All-carbon-based porous topological semimetal for Li-ion battery anode material, Proc. Natl. Acad. Sci. USA **114**, 651 (2017).

[11] Y. Qie, J. Liu, X. Li, S. Wang, Q. Sun, and P. Jena, Interpenetrating silicene networks: A topological nodal-line semimetal with potential as an anode material for sodium ion batteries, Phys. Rev. Mater. **2**, 084201 (2018).

[12] H. Xie, Y. Qie, I. Muhammad, and Q. Sun, B_4 cluster-based 3D porous topological metal as an anode material for both Li- and Na-ion batteries with a superhigh capacity, J. Phys. Chem. Lett. **12**, 1548 (2021).

[13] J. Hu, C. Zhong, W. Wu, N. Liu, Y. Liu, S. A. Yang, and C. Ouyang, 2D honeycomb borophene oxide: A promising anode material offering super high capacity for Li/Na-ion batteries, J. Phys.: Condens. Matter **32**, 65001 (2020).

[14] Z. Ma, F. Wang, M. Dou, Q. Yao, F. Wu, and E. Kan, Boosting the high-capacity with multi-active centers: A first-principles investigation of $NiPS_3$ monolayer as an anode material, Appl. Surf. Sci. **495**, 143534 (2019).

[15] B. Mortazavi, A. Dianat, G. Cuniberti, and T. Rabczuk, Application of silicene, germanene and stanene for Na or Li ion storage: A theoretical investigation, Electrochim. Acta **213**, 865 (2016).

[16] N. K. Jena, R. B. Araujo, V. Shukla, and R. Ahuja, Borophane as a benchmate of graphene: A potential 2D material for anode of Li and Na-ion batteries, ACS Appl. Mater. Interfaces **9**, 16148 (2017).

[17] S. Wang, B. Yang, H. Chen, and E. Ruckenstein, Reconfiguring graphene for high-performance metal-ion battery anodes, Energy Storage Mater. **16**, 619 (2019).

[18] S. Thomas, H. Jung, S. Kim, B. Jun, C. H. Lee, and S. U. Lee, Two-dimensional haeckelite h_{567}: A promising high capacity and fast Li diffusion anode material for lithium-ion batteries, Carbon **148**, 344 (2019).

[19] O. Mashtalir, M. Naguib, V. N. Mochalin, Y. Dall'Agnese, M. Heon, M. W. Barsoum, and Y. Gogotsi, Intercalation and delamination of layered carbides and carbonitrides, Nat. Commun. **4**, 1716 (2013).

[20] M. S. Manju, S. Thomas, S. U. Lee, and A. Kulangara Madam, Mechanically robust, self-healing graphene like defective SiC: A prospective anode of Li-ion batteries, Appl. Surf. Sci. **541**, 148417 (2021).

[21] Y. Dong, W. Wei, X. Lv, B. Huang, and Y. Dai, Semimetallic Si_3C as a high capacity anode material for advanced lithium ion batteries, Appl. Surf. Sci. **479**, 519 (2019).

[22] B. Zhang, Y. Huang, W. Bao, B. Wang, Q. Meng, L. Fan, and Q. Zhang, Two-dimensional stable transition metal carbides (MnC and NbC) with prediction and novel functionalizations, Phys. Chem. Chem. Phys. **20**, 25437 (2018).

[23] C. Zhu, S. Lin, M. Zhang, Q. Li, Z. Su, and Z. Chen, Ultrahigh capacity 2D anode materials for lithium/sodium-ion batteries: An entirely planar B_7P_2 monolayer with suitable pore size and distribution, J. Mater. Chem. A **8**, 10301 (2020).

[24] S. Jana, S. Thomas, C. H. Lee, B. Jun, and S. U. Lee, B_3S monolayer: Prediction of a high-performance anode material for lithium-ion batteries, J. Mater. Chem. A **7**, 12706 (2019).

[25] G. Abbas, S. M. Alay-e-Abbas, A. Laref, Y. Li, and W. X. Zhang, Two-dimensional B_3P monolayer as a superior anode material for Li and Na ion batteries: A first-principles study, Mater. Today Energy **17**, 100486 (2020).

[26] M. Wan, S. Zhao, Z. Zhang, and N. Zhou, Two-dimensional BeB_2 and MgB_2 as high capacity Dirac anodes for Li-ion batteries: A DFT study, J. Phys. Chem. C **126**, 9642 (2022).

[27] X. Lv, F. Li, J. Gong, J. Gu, S. Lin, and Z. Chen, Metallic FeSe monolayer as an anode material for Li and non-Li ion batteries: A DFT study, Phys. Chem. Chem. Phys. **22**, 8902 (2020).

[28] Y. Wang, M. Miao, J. Lv, L. Zhu, K. Yin, H. Liu, and Y. Ma, An effective structure prediction method for layered materials based on 2D particle swarm optimization algorithm, J. Chem. Phys. **137**, 224108 (2012).

[29] Y. Wang, J. Lv, L. Zhu, and Y. Ma, Crystal structure prediction via particle-swarm optimization, Phys. Rev. B **82**, 094116 (2010).

[30] B. Gao, P. Gao, S. Lu, J. Lv, Y. Wang, and Y. Ma, Interface structure prediction via CALYPSO method, Sci. Bull. **64**, 301 (2019).

[31] Y. Wang, J. Lv, L. Zhu, and Y. Ma, CALYPSO: A method for crystal structure prediction, Comput. Phys. Commun. **183**, 2063 (2012).

[32] S. Lin, M. Xu, Z. Qu, Y. Liang, Y. Li, W. Cui, J. Shi, Q. Zeng, J. Hao, and Y. Li, Hidden porous boron nitride as a high-efficiency membrane for hydrogen purification, Phys. Chem. Chem. Phys. **22**, 22778 (2020).

[33] Y. Li, Y. Wang, C. J. Pickard, R. J. Needs, Y. Wang, and Y. Ma, Metallic icosahedron phase of sodium at terapascal pressures, Phys. Rev. Lett. **114**, 125501 (2015).

[34] J. Shi, W. Cui, J. Hao, M. Xu, X. Wang, and Y. Li, Formation of ammonia-helium compounds at high pressure, Nat. Commun. **11**, 3164 (2020).

[35] M. Xu, C. Huang, Y. Li, S. Liu, X. Zhong, P. Jena, E. Kan, and Y. Wang, Electrical control of magnetic phase transition in a type-I multiferroic double-metal trihalide monolayer, Phys. Rev. Lett. **124**, 067602 (2020).

[36] W. Kohn and L. J. Sham, Self-consistent equations including exchange and correlation effects, Phys. Rev. **140**, A1133 (1965).

[37] J. P. Perdew, K. Burke, and M. Ernzerhof, Generalized gradient approximation made simple, Phys. Rev. Lett. **77**, 3865 (1996).

[38] G. Kresse, *Ab initio* molecular dynamics for liquid metals, J. Non. Cryst. Solids **192–193**, 222 (1995).

[39] P. E. Blöchl, Projector augmented-wave method, Phys. Rev. B **50**, 17953 (1994).

[40] H. J. Monkhorst and J. D. Pack, Special points for Brillouin-zone integrations, Phys. Rev. B **13**, 5188 (1976).

[41] A. Togo, F. Oba, and I. Tanaka, First-principles calculations of the ferroelastic transition $CaCl_2$-type SiO_2 at high pressures, Phys. Rev. B **78**, 134106 (2008).

[42] S. Plimpton, Fast parallel algorithms for short-range molecular dynamics, J. Comput. Phys. **117**, 1 (1995).

[43] M. Parrinello and A. Rahman, Crystal structure and pair potentials: A molecular-dynamics study, Phys. Rev. Lett. **45**, 1196 (1980).

[44] J. Klimeš, D. R. Bowler, and A. Michaelides, Van der Waals density functionals applied to solids, Phys. Rev. B **83**, 195131 (2011).

[45] G. Henkelman, B. P. Uberuaga, and H. Jónsson, A climbing image nudged elastic band method for finding saddle points and minimum energy paths, J. Chem. Phys. **113**, 9901 (2000).

[46] See Supplemental Material at http://link.aps.org/supplemental/10.1103/PhysRevResearch.6.013028 for 2D ELF, phonon dispersion curve, MD simulations, adsorption sites, and electronic band structures of BeN monolayer; summaries of the diffusion barrier, OCV, theoretical specific capacity, and energy density of 2D representative materials for Li-ion batteries; the most energetic configurations of solvent molecules and metal salts absorbed on the BeN surface; absorption sites, phonon dispersion curves, MD simulations, electronic band structures and projected density of states, and diffusion pathways of Be_3N_4 and Be_2N_3 monolayers; the optimized structural parameters, Bader charge analysis, elastic constants, calculated E_{ad}, and formation energies of Be_xN_y.

[47] A. D. Becke and K. E. Edgecombe, A simple measure of electron localization in atomic and molecular systems, J. Chem. Phys. **92**, 5397 (1990).

[48] G. Henkelman, A. Arnaldsson, and H. Jónsson, A fast and robust algorithm for Bader decomposition of charge density, Comput. Mater. Sci. **36**, 354 (2006).

[49] F. Mouhat and F.-X. Coudert, Necessary and sufficient elastic stability conditions in various crystal systems, Phys. Rev. B **90**, 224104 (2014).

[50] S. Lei, X. Chen, B. Xiao, W. Zhang, and J. Liu, Excellent electrolyte wettability and high energy density of B_2S as a two-dimensional Dirac anode for non-lithium-ion batteries, ACS Appl. Mater. Interfaces **11**, 28830 (2019).

[51] F. Wang, M. Xu, S. Lin, J. Hao, Y. Wang, H. J. Zhao, and Y. Li, Be_2C_5 monolayer with quasiplanar pentacoordinate carbon atoms and ultrahigh energy density as a Dirac anode for potassium-ion batteries, PRX Energy **2**, 033012 (2023).

[52] X. Gao, Y.-N. Zhou, D. Han, J. Zhou, D. Zhou, W. Tang, and J. B. Goodenough, Thermodynamic understanding of Li-dendrite formation, Joule **4**, 1864 (2020).

[53] L. Shao, X. Duan, Y. Li, F. Zeng, H. Ye, C. Su, and P. Ding, Two-dimensional planar BGe monolayer as an anode material for sodium-ion batteries, ACS Appl. Mater. Interfaces **13**, 29764 (2021).

[54] W. C. Sun, S. S. Wang, and S. Dong, Two-dimensional metallic BP as anode material for lithium-ion and sodium-ion batteries with unprecedented performance, J. Mater. Sci. **56**, 13763 (2021).

[55] Y. Cao, M. Li, J. Lu, J. Liu, and K. Amine, Bridging the academic and industrial metrics for next-generation practical batteries, Nat. Nanotechnol. **14**, 200 (2019).

[56] W. Li, X. Sun, and Y. Yu, and Ge- Si-, Sn-based anode materials for lithium-ion batteries: From structure design to electrochemical performance, Small Methods **1**, 1600037 (2017).

[57] J. Zhang, Y.-F. Zhang, Y. Li, Y.-R. Ren, S. Huang, W. Lin, and W.-K. Chen, Blue-AsP monolayer as a promising anode material for lithium- and sodium-ion batteries: A DFT study, Phys. Chem. Chem. Phys. **23**, 5143 (2021).

[58] C. Yang, X. Zhang, J. Ma, B. Shi, H. Zhang, L. Xu, J. Yang, S. Liu, R. Quhe, and F. Pan, Ultrahigh capacity of monolayer dumbbell C_4N as a promising anode material for lithium-ion battery, J. Electrochem. Soc. **167**, 20538 (2020).

[59] K. Esackraj, N. V. R. Nulakani, V. S. K. Choutipalli, C. Chowdhury, P. Murugan, V. G. Vaidyanathan, and V. Subramanian, Acetylene-mediated borophosphene Dirac materials as efficient anode materials for lithium-ion batteries, ChemPhysChem **24**, e202300035 (2023).

[60] W. L. Du, L. Chen, J. Y. Guo, and H. B. Shu, Novel borophosphene as a high capacity anode material for Li-ion storage, J. Solid State Chem. **296**, 121950 (2021).

[61] M. Xie, J. Pang, W. Jin, and X. Kuang, Theoretical prediction of two-dimensional metal boride Mg_4B_6 as a high-capacity

electrode material for lithium-ion batteries, J. Phys. Chem. C **126**, 17474 (2022).

[62] Y. Kuai, C. Chen, S. Gao, W. Chen, J. Hao, G. Wu, F. Chen, S. Guo, L. Wu, and P. Lu, Two-dimensional SiP_3 monolayer as promising anode with record-high capacity and fast diffusion for alkali-ion battery, Appl. Surf. Sci. **586**, 152510 (2022).

[63] T. Zhang, Y. Ma, B. Huang, and Y. Dai, Two-dimensional penta-BN_2 with high specific capacity for Li-ion batteries, ACS Appl. Mater. Interfaces **11**, 6104 (2019).

[64] C. Zhu, X. Qu, M. Zhang, J. Wang, Q. Li, Y. Geng, Y. Ma, and Z. Su, Planar NiC_3 as a reversible anode material with high storage capacity for lithium-ion and sodium-ion batteries, J. Mater. Chem. A **7**, 13356 (2019).

[65] K. H. Yeoh, K.-H. Chew, Y. Z. Chu, T. L. Yoon, Rusi, and D. S. Ong, First-principles study of monolayer Be_2C as an anode material for lithium-ion batteries, J. Appl. Phys. **126**, 125302 (2019).

[66] Q. H. Qiu, S. Y. Wu, G. J. Zhang, L. Yan, and Z. T. Wei, First-principles studies of the two-dimensional 1*H*-BeP_2 as an electrode material for rechargeable metal ion (Li^+, Na^+, K^+) batteries, Comput. Mater. Sci. **216**, 111868 (2023).

[67] D. Fan, C. Chen, S. Lu, X. Li, M. Jiang, and X. Hu, Highly stable two-dimensional iron monocarbide with planar hypercoordinate moiety and superior Li-ion storage performance, ACS Appl. Mater. Interfaces **12**, 30297 (2020).

[68] S. Wang, Y. Wu, X. Ye, and S. Sun, Predict low energy structures of BSi monolayer as high-performance Li/Na/K ion battery anode, Appl. Surf. Sci. **609**, 155222 (2023).

[69] X. Zhang, L. Jin, X. Dai, G. Chen, and G. Liu, Two-dimensional GaN: An excellent electrode material providing fast ion diffusion and high storage capacity for Li-ion and Na-ion batteries, ACS Appl. Mater. Interfaces **10**, 38978 (2018).

[70] X. Zhang, W. Meng, T. He, L. Jin, X. Dai, and G. Liu, Mn_2C monolayer: A superior anode material offering good conductivity, high storage capacity and ultrafast ion diffusion for Li-ion and Na-ion batteries, Appl. Surf. Sci. **503**, 144091 (2020).

[71] K. Belasfar, M. Houmad, M. Boujnah, A. Benyoussef, and A. EL Kenz, First-principles study of BC_3 monolayer as anodes for lithium-ion and sodium-ion batteries applications, J. Phys. Chem. Solids **139**, 109319 (2020).

[72] X. Zhou, X. Chen, C. Shu, Y. Huang, B. Xiao, W. Zhang, and L. Wang, Two-dimensional boron-rich monolayer B_xN as high capacity for lithium-ion batteries: A first-principles study, ACS Appl. Mater. Interfaces **13**, 41169 (2021).

[73] J. Zhang, L. Xu, C. Yang, X. Zhang, L. Ma, M. Zhang, and J. Lu, Two-dimensional single-layer PC_6 as promising anode materials for Li-ion batteries: The first-principles calculations study, Appl. Surf. Sci. **510**, 145493 (2020).

[74] K. Rajput, V. Kumar, S. Thomas, M. A. Zaeem, and D. R. Roy, Ca_2C MXene monolayer as a superior anode for metal-ion batteries, 2D Mater. **8**, 35015 (2021).

[75] Q. Sun, Y. Dai, Y. Ma, T. Jing, W. Wei, and B. Huang, *Ab initio* prediction and characterization of Mo_2C monolayer as anodes for lithium-ion and sodium-ion batteries, J. Phys. Chem. Lett. **7**, 937 (2016).

[76] H. Zhang, J. Ren, R.-P. Ren, and Y.-K. Lv, Theoretical study of a novel porous penta-TaB with two-dimensional furrow surface as an anode for lithium-ion batteries, New J. Chem. **47**, 9852 (2023).

[77] N. Khossossi, A. Banerjee, Y. Benhouria, I. Essaoudi, A. Ainane, and R. Ahuja, *Ab initio* study of a 2D *H*-BAs monolayer: A promising anode material for alkali-metal ion batteries, Phys. Chem. Chem. Phys. **21**, 18328 (2019).

[78] X. Zhang, C. Yang, Y. Pan, M. Weng, L. Xu, S. Liu, J. Yang, J. Yan, J. Li, B. Shi *et al.*, Monolayer GaS with high ion mobility and capacity as a promising anode battery material, J. Mater. Chem. A **7**, 14042 (2019).

[79] X. Lv, W. Wei, Q. Sun, L. Yu, B. Huang, and Y. Dai, Sc_2C as a promising anode material with high mobility and capacity: A first-principles study, Chem. Phys. Chem. **18**, 1627 (2017).

[80] L. Chen, W. Du, J. Guo, H. Shu, Y. Wang, and J. Dai, Modelling of monolayer penta-PtN_2 as an anode material for Li/Na-ion storage, Mater. Chem. Phys. **262**, 124312 (2021).

[81] D. Chodvadiya, U. Jha, P. Śpiewak, K. J. Kurzydłowski, and P. K. Jha, Potential anodic application of 2D *H*-AlC for Li and Na-ions batteries, Appl. Surf. Sci. **593**, 153424 (2022).

[82] H. Pan, Electronic properties and lithium storage capacities of two-dimensional transition-metal nitride monolayers, J. Mater. Chem. A **3**, 21486 (2015).

[83] J. Xu, J. Mahmood, Y. Dou, S. Dou, F. Li, L. Dai, and J. B. Baek, 2D frameworks of C_2N and C_3N as new anode materials for lithium-ion batteries, Adv. Mater. **29**, 1 (2017).

[84] W. Nong, Y. Li, and C. Wang, C_3N monolayer with substitutional doping and strain modulation serving as anode material of lithium-ion batteries, Appl. Surf. Sci. **510**, 145324 (2020).

[85] Y. Jing, Z. Zhou, C. R. Cabrera, and Z. Chen, Metallic VS_2 monolayer: A promising 2D anode material for lithium ion batteries, J. Phys. Chem. C **117**, 25409 (2013).

[86] Y. Guo, T. Bo, Y. Wu, J. Zhang, Z. Lu, W. Li, X. Li, P. Zhang, and B. Wang, YS_2 monolayer as a high-efficient anode material for rechargeable Li-ion and Na-ion batteries, Solid State Ion. **345**, 115187 (2020).

[87] D. H. Jeon, Wettability in electrodes and its impact on the performance of lithium-ion batteries, Energy Storage Mater. **18**, 139 (2019).

[88] A. Bafekry, C. Stampfl, M. Faraji, M. Yagmurcukardes, M. M. Fadlallah, H. R. Jappor, M. Ghergherehchi, and S. A. H. Feghhi, A Dirac-semimetal two-dimensional BeN_4: Thickness-dependent electronic and optical properties, Appl. Phys. Lett. **118**, 2 (2021).

[89] M. Bykov, T. Fedotenko, S. Chariton, D. Laniel, K. Glazyrin, M. Hanfland, J. S. Smith, V. B. Prakapenka, M. F. Mahmood, A. F. Goncharov *et al.*, High-pressure synthesis of Dirac materials: Layered van der Waals bonded BeN_4 polymorph, Phys. Rev. Lett. **126**, 175501 (2021).

[90] C. Zhang and Q. Sun, A honeycomb BeN_2 sheet with a desirable direct band gap and high carrier mobility, J. Phys. Chem. Lett. **7**, 2664 (2016).

[91] X. Xin, W. Li, R. Pang, H. Wang, C. Guo, X. Shi, and Y. Zhao, Robust ferromagnetism and half-metallicity in fluorinated two-dimensional BeN_2 sheets, Appl. Phys. Lett. **111**, 0 (2017).

[92] Y. Wei, Y. Ma, W. Wei, M. Li, B. Huang, and Y. Dai, Promising photocatalysts for water splitting in BeN_2 and MgN_2 monolayers, J. Phys. Chem. C **122**, 8102 (2018).

[93] Y. Ding, Y. Ji, H. Dong, N. Rujisamphan, and Y. Li, Electronic properties and oxygen reduction reaction catalytic activity of *H*-BeN_2 and MgN_2 by first-principles calculations, Nanotechnology **30**, 465202 (2019).

[94] M. R. A. Kishore, R. Varunaa, A. Bayani, and K. Larsson, Theoretical investigation on BeN_2 monolayer for an efficient bifunctional water splitting catalyst, Sci. Rep. **10**, 24111 (2020).

[95] F. Li, Y. Wang, H. Wu, Z. Liu, U. Aeberhard, and Y. Li, Benzene-like N_6 rings in a Be_2N_6 monolayer: A stable 2D semiconductor with high carrier mobility, J. Mater. Chem. C **5**, 11515 (2017).